Publication Year	2021
Acceptance in OA	2022-03-28T14:43:16Z
Title	GIARPS High-resolution Observations of T Tauri stars (GHOsT). III. A pilot study of stellar and accretion properties
Authors	ALCALA', JUAN MANUEL, Gangi, Manuele Ettore, BIAZZO, Katia, ANTONIUCCI, Simone, FRASCA, Antonio, GIANNINI, Teresa, MUNARI, Ulisse, NISINI, Brunella, Harutyunyan, A., Manara, C. F., VITALI, Fabrizio
Publisher's version (DOI)	10.1051/0004-6361/202140918
Handle	http://hdl.handle.net/20.500.12386/31968
Journal	ASTRONOMY & ASTROPHYSICS
Volume	652

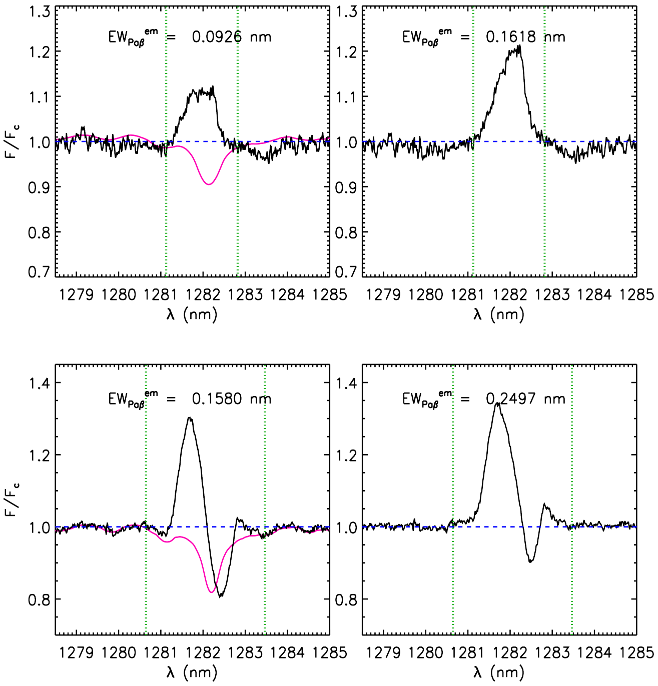

Fig. 6. Examples of photospheric line subtraction for the Paβ line for CQ Tau (upper panels) and RY Tau (lower panels). The red lines represent the photospheric templates. The left and right panels show, in black lines, the observed and photospheric-subtracted spectra, respectively. The green vertical lines mark the intervals for the equivalent width measurement. The equivalent widths of the emission line before and after the subtraction are also indicated.

mainly because of large residuals of telluric lines and/or a strong contribution of the nonphotospheric self-absorption component. DL Tau is the only star for which the complete set of lines could be detected and measured, while CQ Tau has the lowest number of lines with measured fluxes. For most stars, fluxes have been measured for more than 12 lines. In the case of RW Aur A, the Balmer lines higher than H4 (Hγ, Hδ) are dominated by a nonphotospheric self-absorption component. Therefore, we did not attempt a measurement of the flux of those lines. Also, the Hα and Hβ lines in this star may be affected by a similar self-absorption, but we measured their flux with the awareness that it may be underestimated. A contribution of absorption components in the emission lines of DG Tau, DL Tau, HN Tau A, and DO Tau is not significant, and therefore we use the flux measured directly by the integration of the lines. The observed fluxes, equivalent widths, and their errors are reported in several tables provided in Appendix B (Tables B.1 to B.5) [2].

The luminosity of the different emission lines was computed as $L_{\rm line} = 4\pi d^2 \cdot f_{\rm line}$, where d is the YSO distance listed in Table 1 and $f_{\rm line}$ is the extinction-corrected flux of the lines.

4.2. Accretion luminosity

We derived $L_{\rm acc}$ via empirical relationships between accretion luminosity and the luminosity of permitted emission lines. Such relationships have been derived by several authors (e.g., Herczeg & Hillenbrand 2008; Rigliaco et al. 2012; Alcalá et al. 2014, 2017). Here we used the most recent ones by Alcalá et al. (2017), where the relationships are simultaneously derived for lines from the UV to the NIR for a more than 90% complete sample of Lupus YSOs.

Table 4. Summary of the number of lines used to derive the average $L_{\rm acc}$ and accretion properties.

Name	No. lines	log⟨$L_{\rm acc}$⟩ (±σ dex) ($L_\odot$)	⟨$L_{\rm acc}$⟩/$L_\star$	log$\dot{M}_{\rm acc}$ ($M_\odot$ yr^{-1})
RY Tau	12	−0.38 (0.15)	0.05	−7.57
DG Tau	14	−0.25 (0.18)	1.28	−7.35
DL Tau	17	−0.35 (0.18)	1.12	−7.62
HN Tau A†	15	−0.99 (0.23)	0.68	−8.50
DO Tau	16	−0.84 (0.16)	0.34	−7.73
RW Aur A	15	+0.39 (0.30)	1.50	−6.93
CQ Tau	9	−1.18 (0.17)	0.02	−8.68

Notes.
† : subluminous YSO. The values for the accretion properties may be underestimated (see Sect. 4.3.1). Corrected values are provided in Table 5.

In Figure 7 the derived $L_{\rm acc}$ values are plotted as a function of the line diagnostics for the seven targets. The error bars include the errors in $L_{\rm line}$, as well as the errors in each $L_{\rm acc}$–$L_{\rm line}$ calibration. The individual $L_{\rm acc}$ values corresponding to each diagnostic are reported in the various tables in the Appendix B (Tables B.1 to B.5) for every CTT in the sample. An average accretion luminosity, ⟨$L_{\rm acc}$⟩, was then calculated for each target. These values are reported in Table 4 together with the corresponding ⟨$L_{\rm acc}$⟩/$L_\star$ ratio.

The typical standard deviation of ~0.25 dex on log⟨$L_{\rm acc}$⟩ is within the expected error estimated from the fit of the UV continuum excess emission in other samples using slab models (see Alcalá et al. 2014, 2017; Manara et al. 2017a), although the error on $L_{\rm acc}$ for the individual diagnostics is larger than this value. This confirms that the average $L_{\rm acc}$, derived from several diagnostics measured simultaneously, has a significantly reduced error.

4.3. Mass accretion rate

The average accretion luminosity of each target (see Table 4) was converted into mass accretion rate, $\dot{M}_{\rm acc}$, using the relation

$$\dot{M}_{acc} = (1 - \frac{R_\star}{R_{\rm in}})^{-1} \, \frac{\langle L_{acc}\rangle R_\star}{GM_\star} \approx 1.25 \, \frac{\langle L_{acc}\rangle R_\star}{GM_\star}, \quad (1)$$

assuming $\frac{R_\star}{R_{\rm in}} = \frac{1}{5}$, where $R_\star$ and $R_{\rm in}$ are the stellar radius and inner-disk radius, respectively (see Gullbring et al. 1998; Hartmann 1998), and using the stellar parameters reported in Table 2. The resulting $\dot{M}_{\rm acc}$ values are reported in Table 4.

The sources of error in $\dot{M}_{\rm acc}$ are the uncertainties on $L_{\rm acc}$, stellar mass, and radius. Propagating these, we estimate an average error of ~0.35 dex in $\dot{M}_{\rm acc}$ (see Appendix A of Alcalá et al. 2017). However, additional errors on these quantities come from the uncertainty in distance, as well as from differences in the adopted evolutionary tracks. The largest uncertainty on the YSOs distance from the Gaia EDR3 is estimated to be less than ~10%, yielding relative uncertainty of ~0.2 dex in the

---

[2] The flux errors reported in these tables are those resulting from the uncertainty in continuum placement. The estimated ~20% uncertainty of flux calibration (see Sect. 2.2) should be added in quadrature.

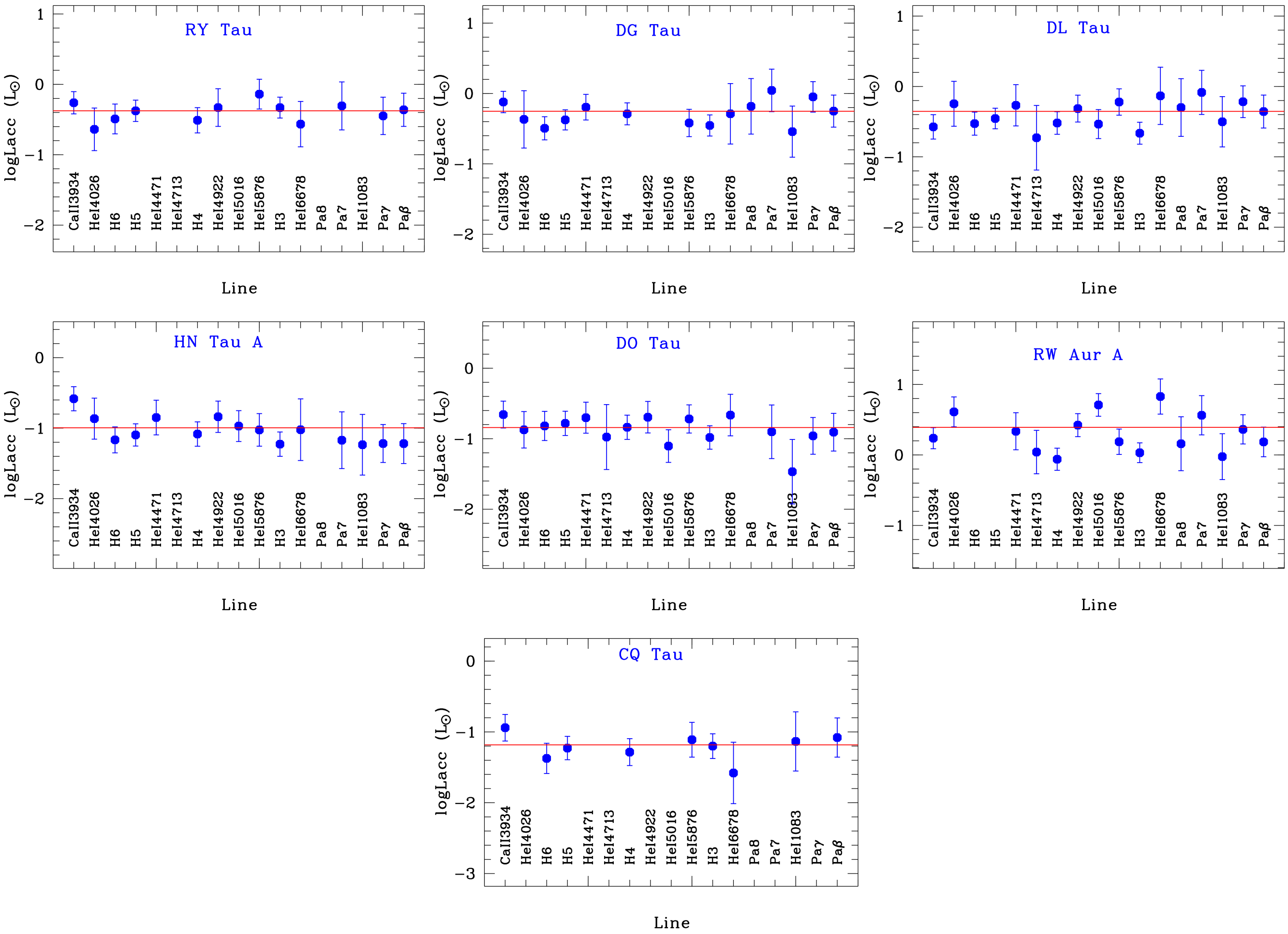

Fig. 7. Plots of $L_{\rm acc}$ as a function of the different accretion diagnostic as labeled for the seven targets (blue dots). The vertical error bars consider the error in $L_{\rm line}$ as well as the errors in the $L_{\rm acc}$–$L_{\rm line}$ relationships. The horizontal red lines in each panel represent the average $L_{\rm acc}$.

mass accretion rate[3]. On the other hand, it has been shown (see Appendix A in Alcalá et al. 2017) that using different sets of PMS evolutionary tracks leads to uncertainties of 0.04 dex to 0.3 dex in $\dot{M}_{\rm acc}$. We therefore estimate that the cumulative relative uncertainty in $\dot{M}_{\rm acc}$ is about 0.4 dex.

We note that our $L_{\rm acc}$= 0.08 $L_\odot$ for CQ Tau is more than an order of magnitude lower than the value reported in Donehew & Brittain (2011, $L_{\rm acc}$=3.8 $L_\odot$; see also Tables 1 and 4 for the $\dot{M}_{\rm acc}$ estimates). Yet, using the Brγ luminosity reported by these authors and the Alcalá et al. (2017) relationships we derive a $L_{\rm acc}$=0.15 $L_\odot$, which is only a factor two our value and within the limits of long-timescale variable accretion (<0.4 dex, see Costigan et al. 2012, 2014). A correction estimate due to UX Ori-type variability yields a $L_{\rm acc}\sim$ 0.38 $L_\odot$ for CQ Tau (see Section 4.3.1), which is still lower by an order of magnitude than the Donehew & Brittain (2011) determination. It is worth noting that our estimate of log$\dot{M}_{\rm acc}$= −8.68 for this star is consistent with the upper limit derived by Mendigutía et al. (2011, log$\dot{M}_{\rm acc}$< −8.3), suggesting that these latter authors also observed the star in its faint phase.

We also stress that the $L_{\rm acc}$ values derived here for RY Tau, DL Tau, HN Tau A, and DO Tau are consistent, within the errors, with those by Ingleby et al (2009) and Ingleby et al. (2012), although in the case of RY Tau our value is a factor of about four lower. We think this may be due to variable accretion. It is also worth mentioning that our $\dot{M}_{\rm acc}$ estimates for RY Tau and DG Tau are in good agreement with the range of values derived by Frasca et al. (2018) based on the Hα and He I 6678 emission lines.

4.3.1. The cases of HN Tau A and CQ Tau

The highly inclined disk of HN Tau A may occult, at least partially, the emission from the accretion flows and from the shock onto the stellar surface, and therefore $L_{\rm acc}$ for this star will be underestimated in a similar way to the $L_\star$ value (see Sect. 3.4). Nevertheless, the $L_{\rm acc}/L_\star$ ratio for this star is at the level of the highest accretors, possibly showing that both $L_{\rm acc}$ and $L_\star$ of the star are obscured in the same manner. This interpretation has proven to be correct for subluminous objects in Lupus (see Sect. 7.4 in Alcalá et al. 2014).

Following the same reasoning as in Alcalá et al. (2020, their Appendix C), we can use the luminosity of the [O I] λ6300 line to estimate a correction factor on $L_{\rm acc}$ and $L_\star$. The [O I] line is found to originate relatively far from the star and there-

---

[3] We note that $\dot{M}_{\rm acc} \propto$ d^3, as $L_{\rm acc} \propto$ d^2 and $R_\star \propto$ d.

Table 5. Accretion and stellar properties of HN Tau A after and before correction for obscuration effects and upper limits for CQ Tau derived as explained in Section 4.3.1.

	HN Tau A		CQ Tau	
Quantity	Corrected with $L^{LVC}_{[\mathrm{O\,I}]}$	Measured values	Upper lim. with ΔB	Measured values
$\log L_{\rm acc}$	-0.12	-0.99	< -0.42	-1.18
$\log L_\star$	$+0.42$	-0.82	$< +1.18$	$+0.43$
$\log R_\star$	$+0.41$	-0.22	$< +0.44$	$+0.07$
$\log M_\star$	$+0.20$	-0.10	$< +0.30$	$+0.18$
$\log \dot{M}_{\rm acc}$	-7.19	-8.68	< -7.70	-8.68

fore should not be significantly affected by obscuration effects from the inner disk, and the line luminosity is also correlated with $L_{\rm acc}$ and $L_\star$ (Natta et al. 2014; Nisini et al. 2018). From the HARPS-N spectrum of HN Tau A, we measure a line flux $\mathrm{F}_{[\mathrm{O\,I}]} = 9\times10^{-14}\,\mathrm{erg\,s^{-1}\,cm^{-2}}$ and derive the extinction corrected ($A_{\rm V}$=1.53 mag) flux $\mathrm{F}^{\rm corr}_{[\mathrm{O\,I}]} = 3\times10^{-13}\,\mathrm{erg\,s^{-1}\,cm^{-2}}$. From Paper I we estimate that about one-third of the flux comes from the low-velocity component (LVC), and therefore we derive a line luminosity, in solar units, of $\log L^{LVC}_{[\mathrm{O\,I}]} = -4.2$. Using the $L_{\rm acc}$--$L_{\rm line}$ and $L_{\rm acc}$-$L_\star$ relationships for the LVC[4] derived by Nisini et al. (2018) we estimate the $\log L_{\rm acc}$ and $\log L_\star$ values given in Table 5, which are a factor of approximately 7 and 17 the subluminous values, respectively, meaning that both $L_{\rm acc}$ and $L_\star$ are affected by a similar obscuration factor, which is consistent with the interpretation for subluminous objects (Alcalá et al. 2014). For comparison, we also include the measured values in Table 5. The corrected stellar luminosity implies a stellar radius a factor about 4.3 larger (i.e., 2.6 $R_\odot$), and places the star on the HR diagram in a position consistent with the other CTTs.

Using the corrected $L_\star$ value and the Siess et al. (2000) evolutionary tracks, we estimate a mass of 1.6 $M_\odot$ for HN Tau A, which is a factor of about two higher than the value provided in Table 2. The $\log g = 3.8$ calculated from the corrected radius and mass is consistent with the typical gravity for YSOs, while the subluminous values yield a much higher gravity of $\log g = 4.7$. The corrected $L_{\rm acc}$, $R_\star$, and $M_\star$ values and Eq. 1 would imply a $\log \dot{M}_{\rm acc} \approx -7.3$, that is, HN Tau A would be among the strongest solar-mass accretors in Taurus.

The work by Nisini et al. (2018) also provides $L_{\rm line}$–$M_\star$ and $L_{\rm line}$–$\dot{M}_{\rm acc}$ relationships allowing us to estimate $M_\star$ and $\dot{M}_{\rm acc}$ indirectly from the $\log L^{LVC}_{[\mathrm{O\,I}]}$ value. The results are also provided in Table 5 and are in agreement with the values derived from the evolutionary tracks and Eq. 1.

We warn the reader about the uncertainties on extinction in high-inclination objects. The above calculations for HN Tau A in this section are based on the assumption that the visual extinction of the LVC of the [O I] line is the same as measured for the star, i.e., $A_{\rm V}$=1.53 mag, which is not necessarily true. However, we note that adopting $A_{\rm V}$=0 mag yields a corrected $L_\star$ a factor of about three lower than when assuming $A_{\rm V}$=1.53 mag, which is still underluminous on the HR diagram. On the other hand, a much higher value of $A_{\rm V}$ would make the star unreliably luminous. We therefore conclude that a reasonable value for the visual extinction of the LVC of the [O I] line should be in the range from about 0.7 mag to 2 mag. As explained above, adopting $A_{\rm V}$=1.53 mag yields a corrected $L_\star$=2.6 $L_\odot$, which leads to consistent results on the stellar parameters. We therefore used this value, but warn the reader that the genuine $L_\star$ value might be in the range between ~1.5 $L_\odot$ and ~3.5 $L_\odot$.

For CQ Tau, the [O I] line is barely seen, and therefore we cannot use the above methodologies to correct the stellar and accretion parameters for obscuration effects. However, we can estimate upper limits based on the photometric variations and assuming gray extinction. As pointed out by Dodin & Suslina (2021), CQ Tau did not show variations before 1940 and was approximately constant at B ~9 mag (Grinin et al. 2008). Adopting this value as the unobscured magnitude of the star and based on our B =10.9 mag measurement during the GHOsT observations, we estimate a correction factor on the bolometric flux of the star of ~5.7. This correction provides a maximum bolometric flux, yielding upper limits of 15 $L_\odot$, 2 $M_\odot$ and 2.8 $R_\odot$ for $L_\star$, $M_\star$, and $R_\star$, respectively. These corrected values of $R_\star$ and $M_\star$ yield a $\log g = 3.9$, which is more consistent with the gravity of a YSO than the $\log g = 4.5$ derived from the observed $R_\star$ and $M_\star$ values in Table 2. Assuming that $L_{\rm acc}$ is affected by the same obscuration factor as $L_\star$ (see Section 7.4 in Alcalá et al. 2014), we derive an upper limit of −7.7 for $\log \dot{M}_{\rm acc}$. The estimated upper limits are listed in Table 5.

5. Results and Discussion

The results of the previous sections show that the studied CTTs in Taurus are highly accreting objects. The novel science products and aspects of this pilot study are as follows.

- Contemporaneous low-resolution spectroscopic and photometric observations, allowing an accurate flux calibration of the high-resolution spectroscopy;
- simultaneity of the high-resolution, wide-band spectroscopic observations, from the optical to the NIR;
- simultaneous use of veiling measurements, both in the optical and NIR, to determine $A_{\rm V}$;
- use of more than ten line diagnostics to estimate accretion luminosity, yielding a much reduced error in $L_{\rm acc}$ as compared with determinations using single diagnostics.

All of the above was achieved using well-defined and assessed procedures for deriving the stellar physical and accretion parameters in a self-consistent and homogeneous way. Therefore, the properties derived here can be considered as more robust and reliable than in previous studies. Some limitations to the application of our procedures are related to the extremely veiled CTTs like RW Aur A, but this type of object is not common. We are therefore confident that the same procedures can be applied to the entire GHOsT data sample, which will be presented in forthcoming papers (Gangi et al., in preparation). In the following, we discuss a few aspects of the stellar and accretion properties of our sample, as well as of the continuum excess emission in the NIR of these CTTs.

5.1. Stellar and accretion properties

This GIARPS/TNG pilot study confirms the high levels of accretion of the selected CTTs. It is worth noting from Table 4 that the $L_{\rm acc}/L_\star$ ratio for every CTT in this sample is well above the level of chromospheric noise emission in YSOs (max $(L_{\rm acc}/L_\star)_{\rm noise}$ ≈0.01 Manara et al. 2017). We point out that in

---

[4] We use only the LVC because the HVC may be affected by the fact that the jet is extended. In this case, the relationships found in Nisini et al. (2018) on a sample observed with the X-Shooter instrument might not give a correct value because of the different instrumental FOV used. The LVC does not suffer from this problem because it forms in a compact region.

three sources, namely, DG Tau, DL Tau, and RW Aur A, the total luminosity is accretion dominated (i.e., $L_{\rm acc}/L_\star > 1$), which is more typical of the class I stage of evolution (e.g., Antoniucci et al. 2008, Fiorellino et al., in press).

The most actively accreting object in this sample is RW Aur A. Noteworthy, the recent study by Takami et al. (2020) shows that the star was in its bright stage during the GIARPS observations (13 Nov. 2017). Moreover, from Paper I we know that the magnitude of the star was 10.44 mag in the *V*-band and this is consistent with the high-accretion activity scenario by Takami et al. (2020).

The apparently least active object in the sample is CQ Tau. This might be mostly related to the much higher photospheric flux in comparison with the other objects, as CQ Tau is an intermediate-mass YSO with $T_{\rm eff}$~6800 K. Nevertheless, its $\dot{M}_{\rm acc}$ is comparable with that of many actively accreting stars of similar mass in other star forming regions. Confirming the upper limits derived in Section 4.3.1 as true values would suggest CQ Tau has a similar level of accretion activity to RY Tau. On the other hand, if the determination of $L_{\rm acc}$ based on the [O I] λ6300 line for HN Tau A is correct (see Sect. 4.3.1), this would also be one of the most actively accreting objects in Taurus.

To investigate the levels of accretion in the Taurus subsample in more detail, we use in the following the 90% complete Lupus sample studied in Alcalá et al. (2017) for comparison purposes, but using the rescaled values reported in Appendix A of Alcalá et al. (2019). Given the very small number statistics of this pilot study, we cannot provide any result on the sample as a whole, but only at the level of the individual objects.

5.1.1. Accretion luminosity versus stellar luminosity

Figure 8 shows the accretion luminosity as a function of stellar luminosity for the Lupus sample and the seven Taurus CTTs. While most Lupus objects lie at $L_{\rm acc}/L_\star$ values between 0.01 and 0.1, five of the Taurus CTTs have higher values, between 0.3 and 1.5 (see Table 4). The two CTTs with values compatible with most of the Lupus YSOs are RY Tau and CQ Tau. We note that recent ALMA data have shown that the dusty disk of the latter has a large cavity (R_{cavity} =53 au, Ubeira Gabellini et al. 2019), likely suggesting a transitional disk. Also, in the case of RY Tau, submillimeter data show evidence for a protoplanetary disk with structures such as rings and an inner cavity (Isella et al. 2010; Pinilla et al. 2018; Long et al. 2018). The $L_{\rm acc}/L_\star$ ratio for both CQ Tau and RY Tau is compatible with those of other transitional disks in Lupus.

Tilling et al. (2008) presented simplified stellar evolution calculations for stars subject to time-dependent accretion history, and derived evolutionary tracks on the $L_{\rm acc}$– $L_\star$ diagram for a variety of fractional disk masses, $f_{disk} \equiv M_{disk}/M_\star$, and YSO masses. Alcalá et al. (2014) showed that the relation of the Lupus data in Figure 8 is steeper than the $L_{\rm acc}/L_\star$ =constant lines, more or less following the slope of the Tilling et al. (2008) tracks. These latter authors also concluded that the disks of the Lupus objects with the lowest masses should have masses lower than $0.014 \times M_\star$. The five high accretors in Taurus (DG, DL, HN, DO, and RW) fall, instead, in the region of the diagram consistent with the Tilling et al. (2008) tracks for YSOs of one solar mass and f_{disk} =0.2. These five stars have indeed masses on the order of $1 M_\odot$ hence, according to such tracks one would expect their disk mass to be on the order of $0.2 \times M_\star$. Although a correlation between the total mass of gas+dust in the disk and the stellar mass has not yet been confirmed, correlations between the dust mass in the disk and the stellar mass of YSOs in the Lupus and Chameleon star forming regions have been found (Ansdell et al. 2016; Pascucci et al. 2016).

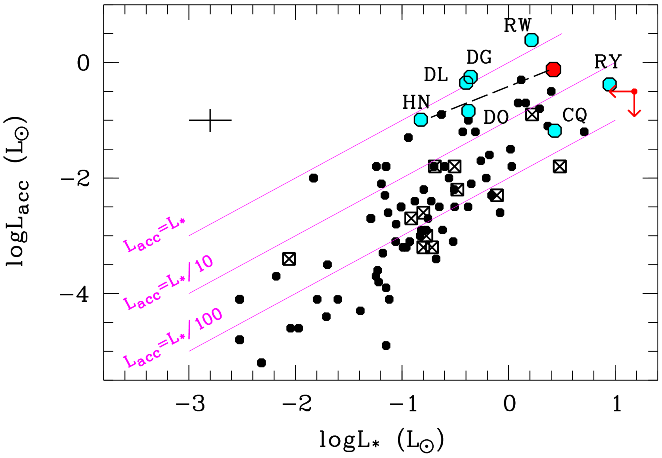

Fig. 8. Accretion luminosity as a function of stellar luminosity for the stars in Lupus (black symbols) and the seven Taurus CTTs studied here (blue circles). The latter are labeled with their names. The Lupus transitional disks are shown with crossed squares. The continuous lines represent the three $L_{\rm acc}$ vs. $L_\star$ relations as labeled. The long-dashed line represents the shift of HN Tau A on the diagram when correcting its $L_{\rm acc}$ and $L_\star$ values for obscuration effects by the disk. The corrected values are shown with the red dot. The leftward and downward red arrows represent the upper limits on $L_\star$ and $L_{\rm acc}$ for CQ Tau, respectively. The average errors for the Taurus sample are shown in the upper left. Figure adapted from Alcalá et al. (2017).

In this scenario, the most massive disk would be RY Tau. The presence of the important jet in RY Tau was recently explained in terms of a very massive disk around this intermediate-mass T Tauri star (Garufi et al. 2019), which might still be fed by the interstellar matter in which the object is embedded. For DG Tau, Podio et al. (2013) estimate a total disk mass in the range 0.015–0.1 $M_\odot$, depending on the assumed dust size distribution. The upper limit would be consistent with the results from the Tilling et al. (2008) tracks. We note that in the case of HN Tau A, the $L_{\rm acc}$ and $L_\star$ values corrected for obscuration effects would still yield similar results for the estimated fractional disk mass, while confirmation of the upper limits for CQ Tau would imply a disk mass similar to that of RY Tau.

5.1.2. Mass accretion rate versus stellar mass

The relationship between mass accretion rate and stellar mass is a fundamental aspect of the study of disk evolution in YSOs. During the CTT phase,that is, after the protostar has almost entirely dispersed its envelope but is still actively accreting from the optically thick accretion disk, the stellar mass undergoes negligible changes. Therefore, the $\dot{M}_{\rm acc}$ versus $M_\star$ relation represents a diagnostic tool for the evolution of $\dot{M}_{\rm acc}$ (Clarke & Pringle 2006) and for the process driving disk evolution (Ercolano et al. 2017).

Figure 9 shows the accretion rate as a function of stellar mass for the seven CTTs in Taurus as compared with the Lupus sample. The Taurus CTTs populate the upper right part of the diagram. Most of the Lupus YSOs fall well below the theoretical prediction by Vorobyov & Basu (2009, short-dashed black line), but the latter is relatively consistent with the upper envelope of the Lupus data points distribution. The few Lupus YSOs on the upper envelope of the $\dot{M}_{\rm acc}$–$M_\star$ relationship are the strongest Lupus accretors at a given mass and are also among the most luminous on the HR diagram. Interestingly, the five Taurus CTTs with the highest $L_{\rm acc}/L_\star$ ratios tend to follow the upper envelope[5], which qualitatively is well fitted by the theoretical prediction. These results demonstrate that the level of accretion of these five CTTs is as high as that of the strongest accretors in Lupus (Alcalá et al. 2017).

On the other hand, CQ Tau falls in the lower envelope of the $\dot{M}_{\rm acc}$–$M_\star$ relationship, with its accretion properties more closely resembling those of transitional disks than those of the full disks, while RY Tau follows the $\dot{M}_{\rm acc}$–$M_\star$ trend for the most massive Lupus stars with full disks. Should the upper limits for CQ Tau be confirmed, its accretion properties will be similar to those of RY Tau.

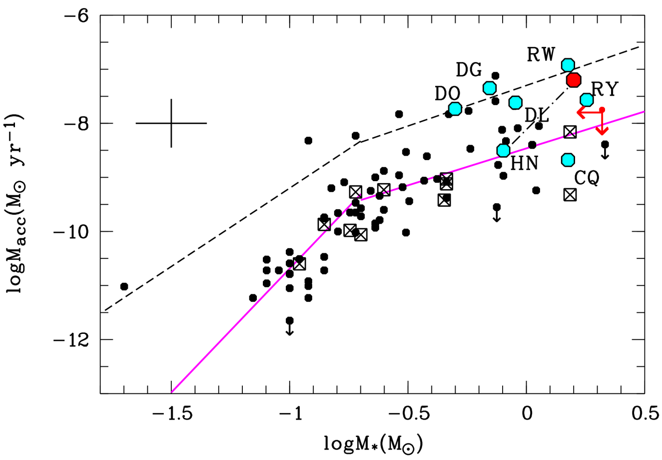

Fig. 9. Mass accretion rate as a function of stellar mass for the seven Taurus CTTs studied (blue circles) compared with stars in Lupus (black symbols). The Lupus transitional disks are shown with crossed squares. Lupus objects classified as weak or negligible accretors are plotted with downward arrows. The long-dashed black line represents the shift of HN Tau A on the diagram when correcting its $\dot{M}_{\rm acc}$ and $M_\star$ values for obscuration effects by the disk. The corrected values are shown with the red dot. The leftward and downward red arrows represent the upper limits on $M_\star$ and $\dot{M}_{\rm acc}$ for CQ Tau, respectively. The black dashed line shows the double power law theoretically predicted by Vorobyov & Basu (2009), and the continuous magenta lines represent the fits to the data as in Eqs. (4) and (5) of Alcalá et al. (2017). The average errors for the Taurus sample are shown in the upper left. Figure adapted from Alcalá et al. (2019).

5.2. The continuum NIR excess emission

Clear evidence of continuum excess emission or veiling increasing with wavelength, from the optical to the NIR, was found in CTTs over a decade ago(Fischer et al. 2011, and references therein). As mentioned in Sect. 3.2, the behavior of IR veiling with wavelength can provide information on the physical properties of the dust in the inner edge of the disk.

Table 6. Results on the veiling emission in the NIR.

Name	$T_{\rm eff}^{\rm BB}$ (K)	F_{factor}^{BB}	R_{sublim} (±err) (au)	R_{in}^{cont} (±err) [a] (au)
RY Tau	1500	51	0.22 (0.05)	0.18 (0.01)
DG Tau	1700	39	0.06 (0.01)	0.17 (0.01)
DL Tau	1600	36	0.06 (0.01)	
HN Tau A	2100	23	0.07 (0.01)†	
DO Tau	1800	25	0.04 (0.01)	
RW Aur A	2150	38	0.07 (0.01)	0.10 (0.01)
CQ Tau	2050	65	0.07 (0.01)	
”	”	”	<0.15‡	
DR Tau	2350	28	0.03 (0.01)	0.12 (0.01)
XZ Tau	1600	29	0.06 (0.01)	

Notes.
† : computed with the $L_\star$ and $L_{\rm acc}$ values in Table 5
‡ : computed with the upper limits on $L_\star$ and $L_{\rm acc}$ in Table 5
a: Interferometric measurements by Eisner et al. (2010)
The values for DR Tau and XZ Tau are taken from Antoniucci et al. (2017)

Figure 10 shows the NIR veiling as a function of wavelength for the seven CTTs in the sample. The increase of veiling with wavelength in the NIR is evident in all the objects. Adopting the same strategies as in Antoniucci et al. (2017), a fit of r$_\lambda$ versus λ with a black-body power law yields the temperature, $T_{\rm eff}^{\rm BB}$, for each CTT indicated in the corresponding panel of Figure 10 and in Table 6. We also include in this table the results for DR Tau and XZ Tau from Antoniucci et al. (2017). Typical errors on the $T_{\rm eff}^{\rm BB}$ are on the order of 100–150 K. The fitting procedure requires another parameter, F_{factor}^{BB}, namely the factor by which the black-body must be multiplied to fit the data. Such a factor is based on the ratio of the areas of the stellar disk and the emitting region producing the NIR veiling. The results using this factor are also given in Table 6. We warn the reader that the fit for DG Tau must be taken with care because only a range of values for the two reddest points could be determined (see Sect. 3.2).

While the resulting temperatures for RY Tau, DG Tau, DL Tau, and within errors DO Tau, are consistent with the origin of the NIR continuum excess emission being the inner rim of the dusty disk, the derived $T_{\rm eff}^{\rm BB}$ value for the other two CTTs is significantly higher than the dust sublimation temperature (∼1500 K) and is more difficult to interpret in the same way, although temperatures as high as 2000 K may be expected for the sublimation of silicate dust (Pollack et al. 1994).

In the simple model by Dullemond et al. (2001), where the inner disk is directly irradiated by the central star, the inner disk edge is located at a radius, R_{sublim}, which is given by the following equation:

$$R_{sublim} = \sqrt{(1+f)\left(\frac{L_\star + L_{acc}}{4\pi\sigma T^4_{sublim}}\right)} \quad , \qquad (2)$$

where f is the ratio of the inner edge height to its radius, and is estimated to be 0.1 for T Tauri stars. Assuming this model and using the $L_\star$ and $L_{\rm acc}$ results of the previous sections, and

---

[5] Here we considered the obscuration corrected quantities for HN Tau A.

adopting $T_{\rm eff}^{\rm BB}$ in Table 6 as sublimation temperature, we computed the R_{sublim} values listed in Table 6 for our sample of CTTs in Taurus. The error in R_{sublim} was calculated by error propagation in Eq. 2 and adopting errors of 0.2 dex, 0.25 dex, and 150 K on $\log L_\star$ $\log L_{\rm acc}$, and $T_{\rm eff}^{\rm BB}$, respectively. We can compare these values with the inner radius, R_{in}^{cont}, derived from interferometric observations of the continuum NIR emission by Eisner et al. (2010) for a few of the CTTs in common. These values are listed in the last column of Table 6. We note that except for RY Tau, where R_{sublim} and R_{in}^{cont} are in very good agreement, the R_{sublim} values for the other four stars with interferometric observations are lower than the R_{in}^{cont} measurements. Interestingly, the upper limits on $L_\star$ and $L_{\rm acc}$ for CQ Tau would yield a R_{sublim} value more similar to those typically found using interferometric observations (see Table 6).

Previous works (i.e., Eisner et al. 2007; Anthonioz et al. 2015) have shown that the irradiated disk model for CTTs predicts radii for the inner rim of the dusty disk that are underestimated with respect to interferometric measurements. We therefore expect the R_{sublim} values in Table 6 for DL Tau, HN Tau A, DO Tau, CQ Tau, and XZ Tau to be underestimated by a factor of between about two and three. However, one possibility is that the $T_{\rm eff}^{\rm BB}$ we measure is not the sublimation temperature, but being instead related to the excess emission in the NIR, may be the temperature of hot gas inside the sublimation radius.

Several authors (e.g., Fischer et al. 2011) discussed possible scenarios for the NIR continuum emission. Among the suggested contributions that may enhance the NIR continuum excess at the shorter IYJ wavelengths there are warm annuli around accretion hot spots, hot gas inside the dust sublimation radius, and hot gas in the accretion flows and/or winds. Fischer et al. (2011) modeled and discussed the presence of multiple temperature components in the shocked photosphere. Also, detailed multiple-component modeling of the accretion emission has been performed by Ingleby et al. (2013).

The results in Paper I showed that DG Tau and HN Tau A share similar physical conditions in their jets. The temperature and ionization gradients of the jets in these two objects would favor a magneto-hydrodynamical shock heating in which the warm and ionized streamlines originate in the internal and mainly gaseous disk, while the low-velocity and almost neutral stream lines come from the dusty regions of the outer disk. Therefore, the hypothesis of a gaseous hot disk inside the dust sublimation radius in HN Tau A and the similarity of the physical conditions of its jet with those in the DG Tau jet would also favor a much higher accretion rate in HN Tau A than what is measured without obscuration correction. The possibility for the formation of the jets in DO Tau and RW Aur A in a gaseous inner disk was also explored in Paper I. In this context, jets signify the presence of dense hot regions inside the gaseous inner disk.

In conclusion, it may be possible that some of the NIR continuum excess emission of the CTTs, in particular in the case of HN Tau A, RW Aur A, and DR Tau, originates in a thick gaseous disk inside the dust sublimation radius, as already suggested by Fischer et al. (2011) and Antoniucci et al. (2017) for other similar cases. In fact, the size of an emitting region estimated as $R_{emiss}^{cont} \sim R_\star \cdot \sqrt{F_{factor}^{BB}}$ is always smaller than the typical inner rim radius of ∼0.1 au in CTTs measured from interferometric observations in the NIR. This is consistent with the results by Koutoulaki et al. (2019) who detected ro-vibrational emission of CO in the NIR X-Shooter spectrum of RW Aur A. The modeling presented by these latter authors of five band-heads shows that the CO emission comes from a region at a distance of ∼0.06–0.08 au from the star.

6. Conclusions

In this pilot study, we report GIARPS@TNG high-resolution observations of seven CTTs in the Taurus-Auriga star forming region, namely RY Tau, DG Tau, DL Tau, HN Tau A, DO Tau, RW Aur A, and CQ Tau. The spectra simultaneously cover a wide spectral range from the optical to the NIR. Contemporaneous spectrophotometric and photometric observations were also performed, allowing us to flux-calibrate the high-resolution spectra with an estimated accuracy of <20%. We show that the GIARPS@TNG data, together with the ancillary observations, allows the stellar and accretion parameters of YSOs to be derived in a self-consistent and homogeneous way.

High-resolution spectroscopy was used to derive the veiling throughout the wide spectral range. The impact of veiling on the estimates of extinction was accounted for. Deriving extinction on the basis of well-flux-calibrated spectral templates alone may lead to underestimation of $A_{\rm V}$ by up to ∼30%, if veiling is neglected. Best matching the spectral type of templates and YSOs reduces errors in the $A_{\rm V}$ estimates. Simultaneously deriving veiling, stellar parameters, and $v \sin i$ avoids degeneracy, which in turn allows more accurate stellar parameters to be obtained.

A large number of emission line diagnostics were used to calculate the accretion luminosity in the seven CTTs via accretion luminosity versus line luminosity relationships. We confirmed that the average $L_{\rm acc}$ derived from several diagnostics measured simultaneously has a significantly reduced error.

We therefore conclude that the GHOsT data sets and the procedures adopted here yield more robust results on the stellar and accretion parameters than those in previous studies of Taurus CTTs. However, in the case of extremely veiled objects, our procedures may fail or provide uncertain results, although this type of object is expected to be rare.

Assuming magnetospheric accretion, we calculated the mass accretion rate of the CTTs in the sample, confirming the high-levels of accretion in these objects. Being in its bright stage during the GIARPS observations, RW Aur A is the most actively accreting object in this sample, which is consistent with the high-accretion activity scenario by Takami et al. (2020). The apparently least active objects in the sample are CQ Tau and HN Tau. We identify these two objects as subluminous on the HR diagram, the former because of its UX Ori-type variability and the latter because of the high inclination of its disk. Correction for disk obscuration makes HN Tau one of the most actively accreting objects in the sample, at a level close to RW Aur A.

A comparison of the accretion properties of the Taurus CTTs with those of Lupus YSOs yields the following results: the Taurus CTTs have values of $L_{\rm acc}/L_\star$ of between 0.3 and 1.5, which are normally higher than those of the Lupus YSOs. The two Taurus objects classified as transitional disks, namely RY Tau and CQ Tau, have values similar to those of the Lupus transitional disks. The five CTTs with the highest $L_{\rm acc}/L_\star$ ratios, namely DG Tau, DL Tau, HN Tau A, DO Tau, and RW Aur A, tend to follow the upper envelope of the $\dot{M}_{\rm acc} - M_\star$ relationship for the Lupus population, and have accretion rates comparable to those of the strongest accretors in Lupus.

The NIR veiling increases with wavelength in all the studied CTTs. The analysis of this behavior shows that these CTTs display a significant continuum excess emission in the NIR. In some cases, such excess can be ascribed to the thermal emission from the inner rim of the dusty disk, while in others may

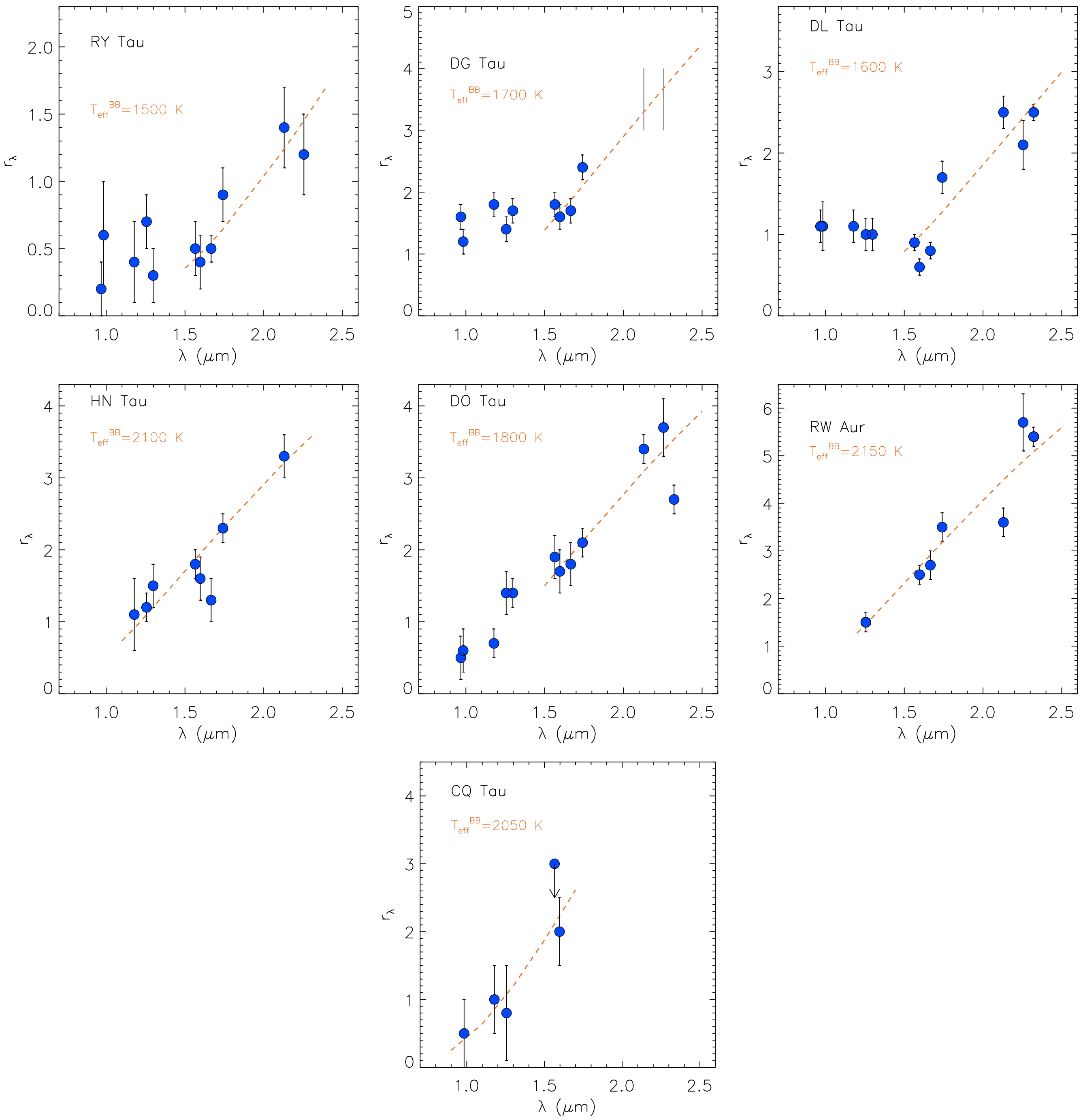

Fig. 10. Plots of NIR veiling as a function of wavelength for the stars in our sample (blue dots). The red dashed lines show the black body fits to the data with $T_{\rm eff}^{\rm BB}$ as labeled. See text for details.

be more compatible with emission from a thick gaseous disk inside the dust sublimation radius. The origin of the jets studied in Paper I is compatible with the latter possibility.

Acknowledgements. We very much thank the anonymous referee for her/his comments and suggestions. This work has been supported by PRIN-INAF-MAIN-STREAM 2017 "Protoplanetary disks seen through the eyes of new-generation instruments" and by PRIN-INAF 2019 "Spectroscopically tracing the disk dispersal evolution (STRADE)". We warmly thank the GAPS team for sharing the solar spectrum acquired with GIARPS, and the TNG personnel for their help during the observations. We dedicate this work to Mr. G.Atusino, whose premature loss deeply saddened all of us; for his immense presence, unconditional support and long-life great friendship. This research made use of the SIMBAD database, operated at the CDS (Strasbourg, France). This work has made use of data from the European Space Agency (ESA) mission *Gaia* (https://www.cosmos.esa.int/gaia), processed by the *Gaia* Data Processing and Analysis Consortium (DPAC, https://www.cosmos.esa.int/web/gaia/dpac/consortium). Funding for the DPAC has been provided by national institutions, in particular the institutions participating in the *Gaia* Multilateral Agreement.

References

Agra-Amboage et al. 2011, A&A, 532, 59
Akeson, R. L., Boden, A. F., Monnier, J. D. et al. 2005, ApJ, 635, 1173
Alcalá, J. M., Natta, A., Manara, C., et al. 2014, A&A, 561, 2
Alcalá, J. M., Manara, C., Natta, A., et al. 2017, A&A, 600, 20
Alcalá, J. M., Manara, C., France, K., et al. 2019, A&A, 629, 108
Alcalá, J. M., Majidi, F.Z., Desidera, S., et al. 2020, A&A, 635, 1
Alencar, S. H. P., Basri, G., Hartmann, L., Calvet, N 2005, A&A, 440, 595
Allard, F., Homeier, D. & Freytag, B. 2012, RSPTA, 370, 2765
Antoniucci, S., Nisini, B., Biazo, K. et al. 2017, A&A, 606, 48
Antoniucci, S., Nisini, B., Giannini, T et al. 2017, A&A,599, 105
Anthonioz, F., Ménard, F., Pinte, C., et al. 2015, A&A, 574, 41
Ansdell, M., Williams, J. P., van der Marel, N. et al. 2016, ApJ, 228,46
Alexander, R. D., Pascucci, I., Andrews, S., Armitage, P., & Cieza, L. 2014, in Protostars and Planets VI, H. Beuther, R. S. Klessen, C. P. Dullemond, & T. Henning (eds.), University of Arizona Press, 475
Andrews, S. M., Wilner, D. J., Espaillat, C., et al. 2011, ApJ, 732, 42
Andrews, S. M., Huang, J., Pérez, L. M. et al. 2018, ApJ, 869, 41
Basri, G. & Batalha, C., 1990, ApJ, 363, 654
Biazzo, K., Randich, S., Palla, F. 2011, A&A, 525, 35
Biazzo, K., Alcalá, J. M., Covino, et al. 2012, A&A, 547, 104
Calvet, N., Muzerolle, J., Briceño, C. et al., 2004, AJ, 128,129
Cardelli, J. A., Clayton, G. C., & Mathis, J. S. 1989, ApJ, 345, 245
Carleo, I., Benatti, S., Lanza, A. F., et al. 2018, A&A, 613, 50A
Claudi, R., Benatti, S., Carleo, I., et al. 2017, EPJP, 132, 364
Clarke, C. J., & Pringle, J. E. 2006, MNRAS, 370, L10
Cody, A. M. & Hillenbrand, L. A. 2010, ApJS, 191, 389
Cosentino, R., Lovis, C., Pepe, F., et al. 2012, in Ground-based and Airbone Instrumentation for Astronomy IV, Proc. SPIE, 8446, 1
Costigan, G., Scholz, A., Stelzer, B., et al. 2012, MNRAS, 427, 1344
Costigan, G., Vink, J. S., Jorick, S., et al. 2014, MNRAS, 440, 3444
Dodin, A. V., Suslina, E. A., 2021, arXiv210208911
Donati, J. F., Landstreet, J. D. 2009, ARA&A, 47, 333
Donehew, B., Brittain, S. 2011, AJ, 141, 46
Dullemond, C. P., Dominik, C., & Natta, A. 2001, ApJ, 560, 95
Eisner, J. A., Hillenbrand, L.A., White, R., J. et al. 2007, ApJ, 669, 1072
Eisner, J. A., Monnier, J.D., Woillez, J. et al. ApJ, 718,774
Ercolano, B., Weber, M.L, & Owen, J.E. 2017, MNRAS, 473, 64
Ercolano, B., Pascucci, I. 2017, RSOS, 470114
Evans, N., J. II et al. 2009, ApJS, 181, 321
Facchini, S., Manara, C. F., Schneider, P. C., et al. 2016, A&A, 596, A38
Fang et al. 2018, ApJ, 868, 28
Fischer, W., Edwards, S., Hillenbrand, L. & Kwan, J. 2011, ApJ, 730, 73
Frasca, A., Guillout, P., Marilli, E., et al. 2006, A&A, 454, 301
Frasca, A., Biazzo, K., Lanzafame, A. C., et al. 2015, A&A575, A4
Frasca, A., Biazzo, K., Alcalá, J. M., et al. 2017, A&A, 602, 33
Frasca, A., Montes, D., Alcalá, J. M., Klutsch, A., Guilloult, P. 2018, Acta Astronomica, 68, 403
Frasca, A., Alonso-Santiago, J., Catanzaro, G., et al. 2019, A&A, 632, A16
Gaia Collaboration; Prusti, T. et al. 2016, A&A, 595, 1
Gaia Collaboration, (Brown, A.G.A, et al.) 2020, arXiv201201533G
Gangi, M., Nisini, B., Antoniucci, S. et al. 2020, A&A, 643, 32
Garufi, A., Podio, L., Bacciotti, F. et al. 2019, A&A, 628, 68
Giannini, T., Nisini, B., Antoniucci, S. et al. 2019, A&A, 631, 44
Gray, D. F. 2005, The Observation and Analysis of Stellar Photospheres, 3rd edn. (Cambridge University Press)
Grinin, V. P., Barsunova, O. Yu., Shugarov, S. Yu. et al. 2008, Astrophysics, 51, 1
Gullbring, E., Hartmann, L., Briceño, C., & Calvet, N. 1998, ApJ, 492, 323
Gullbring, E., et al. 2000, ApJ, 544, 927
Hartigan, P., Kenyon, S. J., Hartmann, L., et al. 1991,ApJ, 382, 617
Hartigan, P., & Kenyon, S. J. 2003, ApJ, 583, 334
Hartmann, L. 1998, in Accretion Processes in Star Formation, Cambridge University Press
Hartmann, L. E., Calvet, N., Gullbring, E., & D'Alessio, P. 1998, ApJ, 495, 385
Hartmann, L., Herczeg, G., Calvet, N. 2016, ARA&A, 54, 135
Herczeg, G., & Hillenbrand, L. A. 2008, ApJ, 681, 594
Herczeg, G., & Hillenbrand, L. A. 2014, ApJ, 786, 97
Hessman, F., Guenther, E. W., 1997, A&A, 321, 497
Ingleby, L., Calvet, N., Bergin, E., et al. 2009, ApJ, 703, 137
Ingleby, L., Calvet, N., Herczeg, G., Briceño, C. 2012, ApJ, 752,20
Ingleby, L., Calvet, N., Herczeg, G. et al. 2013, ApJ, 767, 112
Isella, A., Carpenter, J. M., & Sargent, A. I. 2010, ApJ, 701, 260
Isella, A., Carpenter, J. M., & Sargent, A. I. 2010, ApJ, 714, 1746
Jayawardhana, R., Coffey, J., Scholz, A., Brandeker, A., & van Kerkwijk, M. H. 2006, ApJ, 648, 1206
Johns-Krull, C. M., Chen, W., Valenti, J. A. et al. 2013, ApJ, 765, 11
Kausch, W., Noll, S., Smette, A., et al. 2015, A&A, 576, 78
Kenyon, S, J. Gómez, M., Whitney, B.A., 2008, Handbook of Star Forming Regions, Volume I: The Northern Sky, ASP Monograph Publications, Vol. 5, B. Reipurth (ed.), p. 405
Koutoulaki, M., Facchini, S., Manara, C. F., et al. 2019, A&A, 625, A49
Long, F., Pinilla, P., Herczeg, G. J., et al. 2018, ApJ, 869, 17
Long, F., Herczeg, G. J., Harsono, D. et al. 2019, ApJ, 882, 49
Lynden-Bell, D., & Pringle, J. E. 1974, MNRAS, 168, 603
Manara, C. F., Beccari, G., Da Rio, N., et al. 2013, A&A, 558, 114
Manara, C. F., Rosotti, G., Testi, L. et al. 2016, A&A, 591, L3
Manara, C. F., Frasca, A., Alcalá, J. M., Natta, A., Stelzer, B., Testi, L. 2017, A&A, 605, 86
Manara, C. F., Testi, L., Herczeg, G. J., et al. 2017, A&A, 604, 127
Meeus, G., Montesinos, B., Mendigutía, I. et al. 2012, A&A, 544, 78
Mendigutía, I., Calvet, N., Montesinos, B. et al. 2011, A&A, 535, 99
Morbidelli, A., Raymond, S. N. 2016, JGRE, 121, 1962
Moultaka, J., Ilovaisky, S. A., Prugniel, P., & Soubiran, C. 2004, PASP, 116, 693
Mulders, G. D., Pascucci, I., Manara, C. F., et al. 2017, ApJ, 847, 31
Munari, U., Bacci, S., Baldinelli, L. et al. 2012, Baltic Astronomy, 21, 13
Muzerolle, J., Hartmann, L., & Calvet, N. 1998, AJ, 116, 455
Natta, A., Testi, L., & Randich, S. 2006, A&A, 452, 245
Natta, A., Testi, L., Alcalá, J.M., Rigliaco, E., Covino, E., Stelzer, B., D'Elia, V. 2014, A&A, 569, 5
Nisini, B., Antoniucci, S., Alcalá, J. M., et al. 2018, A&A, 609, 89
Oliva, E., Origlia, L., Maiolino, R., et al. 2012, in Ground-based and Airbone Instrumentation for Astronomy IV, Proc. SPIE, 8446, 3
Origlia, L., Oliva, E., Baffa, C., et al. 2014, in Ground-based and Airbone Instrumentation for Astronomy V, Proc. SPIE, 9147, 1
Pascucci, I., Testi, L., Herczeg, G. J., et al. 2016, ApJ, 831, 125
Pepe, F., Mayor, M., Galland, F., et al. 2002, A&A, 388, 632
Pinilla, P., Tazzari, M., Pascucci, I. et al. 2018, ApJ, 859, 32
Podio, L., Kamp, I., Codella, C. et al. 2013, ApJ, 766, 5
Pollack, J. B., Hollenbach, D., Beckwith, S. et al. 1994, ApJ, 421, 615
Rayner, J. T., Cushing, M. C., & Vacca, W. D. 2009, ApJS, 185, 289
Rigliaco, E., Natta, A., Testi, L., et al. 2012, A&A, 548, A56
Rigliaco, E., Pascucci, I., Duchene, G., et al. 2015, ApJ, 801, 31
Rosotti, G. P., Clarke, C. J., Manara, C. F., & Facchini, S. 2017, MNRAS, 468, 1631
Shakhovskoj, D. N.; Grinin, V. P.; Rostopchina, A. N., 2005, Astrophysics, Volume 48, Issue 2, pp.135-142
Siess, L., Dufour, E., & Forestini, M. 2000, A&A, 358, 593
Simon, M. N., Pascucci, I., Edwards, S., et al. 2016, ApJ, 831, 169
Skinner, S. L., Schneider, P. C., Audard, M., & Güdel, M. 2018, ApJ, 855, 143
Smette, A., Sana, H., Noll, S., et al. 2015, A&A, 576, A77
Stout-Batalha, N. M., Batalha, C. C.; Basri, G. S. 2000, ApJ, 532, 474
Takami, M., Beck, T. L., Schneider, P.C. et al. 2020, ApJ, 901, 24
Tillling, I., Clarke, C. J., Pringle, J. E., & Tout, C. A. 2008, MNRAS, 385, 1530
Ubeira Gabellini, G. M., Miotello, A., Fachini, S. et al. 2019, MNRAS, 486, 4638
Venuti, L., Bouvier, J., Flaccomio, E., et al. 2014, A&A, 570, 82
Vitali, F., Zerbi, F. M., Chincarini, G., et al. 2003, Proc. SPIE, 4841, 627
Vorobyov, E. I., & Basu, S. 2009, ApJ, 703, 922
Weingartner, J. C., & Draine, B. T. 2001, ApJ, 548, 296
White, R. J. & Basri, G. 2003, ApJ, 582, 1109
White, R., & Hillenbrand, L. A. 2004, ApJ, 616, 998
White, R., & Genz, 2011, ApJ, 556, 265

Appendix A: Measurements of continuum fluxes for the CTTs and templates

In Tables A.1 to A.7 we report the observed continuum fluxes for the CTTs and the spectral templates adopted for the determination of the extinction according to the methods described in Fischer et al. (2011). We define the quantity:

$$\Gamma_\lambda \equiv 2.5 \cdot \log\left[(1 + r_\lambda) \cdot \frac{F^T_\lambda}{F^O_\lambda}\right], \tag{A.1}$$

where r_λ, F^T_λ, and F^O_λ are the veiling, the observed continuum flux of the spectral template, and the observed continuum flux of the object, as a function of wavelength, respectively. As mentioned in Sect. 3.3, the method is based on the fact that

$$\Gamma_\lambda = (\mathrm{A_v^O} - \mathrm{A_v^T}) \cdot \frac{\mathrm{A}_\lambda}{\mathrm{A_v}} - 2.5 \cdot \log \mathrm{C}, \tag{A.2}$$

so that Γ_λ is a lineaar function of $\frac{\mathrm{A}_\lambda}{\mathrm{A_v}}$, where $\mathrm{A_v^O}$ and $\mathrm{A_v^T}$ are the visual extinction of the the object and template, respectively, and C is a constant. The tables also provide Γ_λ as a function of wavelength and the r_λ values are also included for convenience.

Table A.1. Γ_λ versus $\mathrm{A}_\lambda/\mathrm{A_v}$ for RY Tau.

Wavelength (nm)	$\mathrm{A}_\lambda/A_\mathrm{V}$	F_λ^T erg/s/cm^2/nm	F_λ^O erg/s/cm^2/nm	r_λ	Γ_λ
450.0	1.169	1.70e-11	2.00e-12	0.0	2.324
500.0	1.080	2.10e-11	2.20e-12	0.0	2.449
550.0	0.990	2.10e-11	2.60e-12	0.0	2.268
600.0	0.900	1.90e-11	3.00e-12	0.0	2.004
650.0	0.820	1.80e-11	3.20e-12	0.0	1.875
968.0	0.450	8.60e-12	5.00e-12	0.2	0.787
983.0	0.430	8.40e-12	5.10e-12	0.6	1.052
1178.0	0.300	5.60e-12	5.30e-12	0.4	0.425
1256.0	0.264	4.90e-12	5.10e-12	0.7	0.533
1298.0	0.250	4.60e-12	4.90e-12	0.3	0.216
1565.0	0.178	2.90e-12	3.50e-12	0.5	0.236
1597.0	0.173	2.80e-12	3.30e-12	0.4	0.187
1666.0	0.163	2.40e-12	2.90e-12	0.5	0.235
1741.0	0.151	2.00e-12	2.40e-12	0.9	0.499
2130.0	0.114	1.00e-12	1.60e-12	1.4	0.440
2255.0	0.110	8.30e-13	2.20e-12	1.2	0.202
2322.0	0.100	7.50e-13	2.80e-12	...	...

Appendix B: Individual fluxes, equivalent widths and L_acc estimates

Tables B.1 to B.5 report the observed fluxes, equivalent widths, for every CTTs in the sample, as well as the corresponding L_acc values derived from the individual accretion diagnostics and using the L_acc–L_line relationships by Alcalá et al. (2017).

Table A.2. Γ_λ versus $\mathrm{A}_\lambda/\mathrm{A_v}$ for DG Tau.

Wavelength (nm)	$\mathrm{A}_\lambda/A_\mathrm{V}$	F_λ^T erg/s/cm^2/nm	F_λ^O erg/s/cm^2/nm	r_λ	Γ_λ
450.0	1.169	4.20e-14	2.20e-13	...	...
500.0	1.080	4.70e-14	2.40e-13	...	...
550.0	0.990	6.90e-14	3.20e-13	2.0	-0.473
600.0	0.900	7.70e-14	3.90e-13	1.5	-0.767
650.0	0.820	8.60e-14	4.60e-13	1.0	-1.068
968.0	0.450	1.00e-13	9.60e-13	1.6	-1.418
983.0	0.430	9.00e-14	9.80e-13	1.2	-1.736
1178.0	0.300	7.00e-14	1.10e-12	1.8	-1.873
1256.0	0.264	6.70e-14	1.10e-12	1.4	-2.088
1298.0	0.250	6.50e-14	1.10e-12	1.7	-1.993
1565.0	0.178	5.50e-14	1.00e-12	1.8	-2.031
1597.0	0.173	5.40e-14	9.90e-13	1.6	-2.121
1666.0	0.163	5.10e-14	9.60e-13	1.7	-2.108
1741.0	0.151	4.50e-14	9.30e-13	2.4	-1.959
2130.0	0.114	2.70e-14	7.90e-13	3.0	-2.161
2255.0	0.110	2.20e-14	7.70e-13	4.0	-2.113
2322.0	0.100	2.00e-14	7.70e-13	...	...

Table A.3. Γ_λ versus $\mathrm{A}_\lambda/\mathrm{A_v}$ for DL Tau.

Wavelength (nm)	$\mathrm{A}_\lambda/A_\mathrm{V}$	F_λ^T erg/s/cm^2/nm	F_λ^O erg/s/cm^2/nm	r_λ	Γ_λ
450.0	1.169	6.10e-13	1.40e-13	3.0	3.103
500.0	1.080	6.20e-13	1.50e-13	2.5	2.901
550.0	0.990	8.90e-13	2.00e-13	2.0	2.814
600.0	0.900	9.00e-13	2.50e-13	1.5	2.386
650.0	0.820	9.60e-13	2.90e-13	1.5	2.295
968.0	0.450	9.50e-13	4.90e-13	1.1	1.524
983.0	0.430	1.00e-12	4.90e-13	1.1	1.580
1178.0	0.300	1.10e-12	4.70e-13	1.1	1.729
1256.0	0.264	1.00e-12	4.70e-13	1.0	1.572
1298.0	0.250	9.70e-13	4.60e-13	1.0	1.563
1565.0	0.178	8.60e-13	4.20e-13	0.9	1.475
1597.0	0.173	8.00e-13	4.10e-13	0.6	1.236
1666.0	0.163	7.80e-13	4.00e-13	0.8	1.363
1741.0	0.151	6.90e-13	3.90e-13	1.7	1.698
2130.0	0.114	3.70e-13	2.90e-13	2.5	1.625
2255.0	0.110	3.10e-13	2.60e-13	2.1	1.419
2322.0	0.100	2.70e-13	2.40e-13	2.5	1.488

Table A.4. Γ_λ versus $\mathrm{A}_\lambda/\mathrm{A_v}$ for HN Tau A.

Wavelength (nm)	$\mathrm{A}_\lambda/A_\mathrm{V}$	F_λ^T erg/s/cm^2/nm	F_λ^O erg/s/cm^2/nm	r_λ	Γ_λ
450.0	1.169	7.50e-13	6.40e-14	...	...
500.0	1.080	7.60e-13	7.40e-14	0.8	3.167
550.0	0.990	8.60e-13	8.80e-14	0.8	3.113
600.0	0.900	9.00e-13	1.00e-13	0.8	3.024
650.0	0.820	8.70e-13	1.10e-13	0.5	2.686
968.0	0.450	5.90e-13	1.50e-13	...	...
983.0	0.430	5.80e-13	1.50e-13	...	...
1178.0	0.300	4.60e-13	1.50e-13	1.1	2.022
1256.0	0.264	4.00e-13	1.40e-13	1.2	1.996
1298.0	0.250	3.80e-13	1.40e-13	1.5	2.079
1565.0	0.178	3.00e-13	1.40e-13	1.8	1.945
1597.0	0.173	2.90e-13	1.40e-13	1.6	1.828
1666.0	0.163	2.70e-13	1.30e-13	1.3	1.698
1741.0	0.151	2.20e-13	1.30e-13	2.3	1.867
2130.0	0.114	1.20e-13	1.30e-13	3.3	1.497
2255.0	0.110	1.00e-13	1.20e-13	5.0	1.747
2322.0	0.100	8.30e-14	1.20e-13	...	...

Table A.5. Γ_λ versus A_λ/A_v for DO Tau.

Wavelength (nm)	A_λ/A_V	F^T_λ erg/s/cm^2/nm	F^O_λ erg/s/cm^2/nm	r_λ	Γ_λ
450.0	1.169	4.60e-14	1.50e-13	1.8	-0.165
500.0	1.080	5.30e-14	1.60e-13	1.5	-0.205
550.0	0.990	7.10e-14	1.80e-13	1.5	-0.015
600.0	0.900	7.80e-14	2.10e-13	1.0	-0.323
650.0	0.820	8.70e-14	2.30e-13	1.5	-0.061
968.0	0.450	9.90e-14	5.00e-13	0.5	-1.318
983.0	0.430	8.90e-14	5.10e-13	0.6	-1.385
1178.0	0.300	7.10e-14	5.80e-13	0.7	-1.704
1256.0	0.264	6.60e-14	6.00e-13	1.4	-1.446
1298.0	0.250	6.40e-14	6.00e-13	1.4	-1.479
1565.0	0.178	5.50e-14	6.10e-13	1.9	-1.456
1597.0	0.173	5.50e-14	6.10e-13	1.7	-1.534
1666.0	0.163	5.20e-14	6.00e-13	1.8	-1.537
1741.0	0.151	4.70e-14	5.90e-13	2.1	-1.518
2130.0	0.114	2.70e-14	4.90e-13	3.4	-1.538
2255.0	0.110	2.10e-14	4.50e-13	3.7	-1.647
2322.0	0.100	1.90e-14	4.30e-13	2.7	-1.966

Table A.6. Γ_λ versus A_λ/A_v for RW Aur A.

Wavelength (nm)	A_λ/A_V	F^T_λ erg/s/cm^2/nm	F^O_λ erg/s/cm^2/nm	r_λ	Γ_λ
450.0	1.169	7.70e-13	2.20e-12	...	...
500.0	1.080	7.50e-13	2.30e-12	...	...
550.0	0.990	7.60e-13	2.20e-12	1.2	-0.298
600.0	0.900	7.10e-13	2.20e-12	...	...
650.0	0.820	6.70e-13	2.30e-12	...	...
968.0	0.450	3.80e-13	1.80e-12	...	...
983.0	0.430	3.70e-13	1.80e-12	...	...
1178.0	0.300	2.60e-13	1.40e-12	...	...
1256.0	0.264	2.30e-13	1.30e-12	1.5	-0.886
1298.0	0.250	2.20e-13	1.30e-12	...	...
1565.0	0.178	1.60e-13	1.00e-12	...	...
1597.0	0.173	1.50e-13	1.00e-12	2.5	-0.700
1666.0	0.163	1.30e-13	9.50e-13	2.7	-0.739
1741.0	0.151	1.10e-13	9.10e-13	3.5	-0.661
2130.0	0.114	5.50e-14	6.60e-13	3.6	-1.041
2255.0	0.110	4.40e-14	5.70e-13	5.7	-0.716
2322.0	0.100	3.70e-14	5.10e-13	5.4	-0.833

Table A.7. Γ_λ versus A_λ/A_v for CQ Tau.

Wavelength (nm)	A_λ/A_V	F^T_λ erg/s/cm^2/nm	F^O_λ erg/s/cm^2/nm	r_λ	Γ_λ
450.0	1.169	7.90e-12	4.90e-12	0.0	0.519
500.0	1.080	7.00e-12	4.60e-12	0.0	0.456
550.0	0.990	6.00e-12	4.30e-12	0.0	0.362
600.0	0.900	5.30e-12	3.90e-12	0.0	0.333
650.0	0.820	4.50e-12	3.40e-12	0.0	0.304
968.0	0.450	1.90e-12	2.60e-12	...	...
983.0	0.430	1.80e-12	2.50e-12	0.5	0.084
1178.0	0.300	1.10e-12	2.00e-12	1.0	0.103
1256.0	0.264	9.50e-13	1.90e-12	0.8	-0.114
1298.0	0.250	8.60e-13	1.80e-12	...	.....
1565.0	0.178	5.00e-13	1.50e-12	<3.0	<0.312
1597.0	0.173	4.80e-13	1.50e-12	2.0	-0.044
1666.0	0.163	4.10e-13	1.50e-12	...	...
1741.0	0.151	3.50e-13	1.40e-12	...	...
2130.0	0.114	1.70e-13	1.20e-12	...	...
2255.0	0.110	1.30e-13	1.10e-12	...	...
2322.0	0.100	1.20e-13	1.10e-12	...	...

Table B.1. Measured fluxes and equivalent widths of Balmer lines and accretion luminosity for the CTTs sample: Hα (H3) to Hδ (H6).

Object	$f_{\mathrm{H}\alpha}$ (erg s^{-1} cm^{-2})	$EW_{\mathrm{H}\alpha}$ (Å)	$f_{\mathrm{H}\beta}$ (erg s^{-1} cm^{-2})	$EW_{\mathrm{H}\beta}$ (Å)	$f_{\mathrm{H}\gamma}$ (erg s^{-1} cm^{-2})	$EW_{\mathrm{H}\gamma}$ (Å)	$f_{\mathrm{H}\delta}$ (erg s^{-1} cm^{-2})	$EW_{\mathrm{H}\delta}$ (Å)
RY Tau	4.78(±0.22)e−12	−14.49±0.54	3.30(±0.56)e−13	−1.72±0.13	2.44(±0.30)e−13	−1.36±0.20	1.54(±0.46)e−13	−0.95±0.14
DG Tau	6.30(±0.09)e−12	−108.43±7.28	1.01(±0.06)e−12	−43.72±8.80	5.02(±0.35)e−13	−33.92±8.01	3.20(±0.27)e−13	−24.81±6.66
DL Tau	3.19(±0.06)e−12	−91.93±6.09	5.41(±0.30)e−13	−39.20±6.85	3.73(±0.33)e−13	−33.30±9.29	2.65(±0.21)e−13	−30.15±7.32
HN Tau A	1.42(±0.02)e−12	−113.60±7.57	2.39(±0.10)e−13	−32.39±4.53	1.36(±0.13)e−13	−25.86±6.27	9.25(±0.96)e−14	−19.64±5.24
DO Tau	1.92(±0.07)e−17	−64.87±6.99	3.10(±0.29)e−13	−19.87±4.51	2.03(±0.39)e−13	−12.69±8.19	1.51(±0.39)e−13	−10.13±8.38
RW Aur A	1.74(±0.02)e−11	−69.88±2.47	2.28(±0.20)e−12	−10.18±1.29	...	...	...	...
CQ Tau	2.29(±0.18)e−12	−7.53±0.42	3.09(±0.45)e−13	−0.83±0.17	2.18(±0.29)e−13	−0.56±0.32	1.29(±0.31)e−13	−0.29±0.10

Object	$\log(L_{\mathrm{acc}}/L_{\odot})$ Hα	$\pm\sigma$ (dex)	$\log(L_{\mathrm{acc}}/L_{\odot})$ Hβ	$\pm\sigma$ (dex)	$\log(L_{\mathrm{acc}}/L_{\odot})$ Hγ	$\pm\sigma$ (dex)	$\log(L_{\mathrm{acc}}/L_{\odot})$ Hδ	$\pm\sigma$ (dex)
RY Tau	−0.33	0.15	−0.51	0.18	−0.38	0.15	−0.49	0.21
DG Tau	−0.45	0.15	−0.29	0.16	−0.38	0.14	−0.50	0.16
DL Tau	−0.67	0.16	−0.52	0.16	−0.46	0.15	−0.53	0.16
HN Tau A	−1.23	0.17	−1.08	0.17	−1.10	0.16	−1.17	0.18
DO Tau	−0.98	0.17	−0.84	0.17	−0.78	0.17	−0.82	0.21
RW Aur A	−0.29	0.14	−0.38	0.16	...	...	...	...
CQ Tau	−1.20	0.17	−1.29	0.17	−1.23	0.17	−1.37	0.21

Table B.2. Measured fluxes and equivalent widths of Paschen lines and accretion luminosity for the CTTs sample: Paβ (Pa5) to Paϵ (Pa8).

Object	$f_{\mathrm{Pa}\beta}$ (erg s^{-1} cm^{-2})	$EW_{\mathrm{Pa}\beta}$ (Å)	$f_{\mathrm{Pa}\gamma}$ (erg s^{-1} cm^{-2})	$EW_{\mathrm{Pa}\gamma}$ (Å)	$f_{\mathrm{Pa}\delta}$ (erg s^{-1} cm^{-2})	$EW_{\mathrm{Pa}\delta}$ (Å)	$f_{\mathrm{Pa}\epsilon}$ (erg s^{-1} cm^{-2})	$EW_{\mathrm{Pa}\epsilon}$ (Å)
RY Tau	1.20(±0.08)e−12	−2.66±0.32	4.92(±1.16)e−13	−1.05±0.35	3.71(±0.71)e−13	−0.80±0.22	...	...
DG Tau	1.98(±0.07)e−12	−18.50±0.98	1.40(±0.02)e−12	−13.33±0.83	1.00(±0.06)e−12	−10.15±0.89	8.01(±1.01)e−13	−7.93±1.67
DL Tau	1.03(±0.07)e−12	−22.01±2.15	6.86(±0.53)e−13	−14.29±1.67	5.37(±0.06)e−13	−10.76±1.72	4.35(±0.81)e−13	-8.19±2.43
HN Tau A	2.28(±0.12)e−13	−16.06±1.26	1.52(±0.17)e−13	−10.41±1.56	9.80(±2.40)e−14	-6.67±2.13	...	...
DO Tau	3.97(±0.33)e−13	-6.64±0.75	2.16(±0.27)e−13	-3.85±0.65	1.42(±0.03)e−13	-2.80±0.76	...	...
RW Aur A	2.80(±0.10)e−12	−21.37±1.24	1.91(±0.11)e−12	−12.99±1.12	1.80(±0.15)e−12	−10.71±1.26	1.13(±0.25)e−12	-6.46±1.88
CQ Tau	3.02(±0.40)e−13	-1.66±0.38	...	...	...	...	...	...

Object	log($L_{\mathrm{acc}}/L_{\odot}$) Pa$\beta$	±σ (dex)	log($L_{\mathrm{acc}}/L_{\odot}$) Pa$\gamma$	±σ (dex)	log($L_{\mathrm{acc}}/L_{\odot}$) Pa$\delta$	±σ (dex)	log($L_{\mathrm{acc}}/L_{\odot}$) Pa$\epsilon$	±σ (dex)
RY Tau	−0.36	0.24	−0.45	0.27	−0.31	0.34	...	...
DG Tau	−0.25	0.23	−0.05	0.22	+0.04	0.30	−0.18	0.40
DL Tau	−0.36	0.23	−0.22	0.23	−0.08	0.31	−0.30	0.41
HN Tau A	−1.22	0.28	−1.22	0.27	−1.17	0.40	...	...
DO Tau	−0.91	0.27	−1.00	0.26	−0.90	0.38	...	...
RW Aur A	+0.19	0.21	+0.36	0.21	+0.56	0.28	+0.16	0.38
CQ Tau	−1.08	0.28	...	...	...	...	...	...

Table B.3. Measured fluxes and equivalent widths of He I lines and accretion luminosity for the CTTs sample: He I 4026 to He I 4922.

Object	$f_{\mathrm{He\,I}\,\lambda4026}$ (erg s^{-1} cm^{-2})	$EW_{\mathrm{He\,I}\,\lambda4026}$ (Å)	$f_{\mathrm{He\,I}\,\lambda4471}$ (erg s^{-1} cm^{-2})	$EW_{\mathrm{He\,I}\,\lambda4471}$ (Å)	$f_{\mathrm{He\,I}\,\lambda4713}$ (erg s^{-1} cm^{-2})	$EW_{\mathrm{He\,I}\,\lambda4713}$ (Å)	$f_{\mathrm{He\,I}\,\lambda4922}$ (erg s^{-1} cm^{-2})	$EW_{\mathrm{He\,I}\,\lambda4922}$ (Å)
RY Tau	1.02(±0.51)e−14	−0.07±0.06	...	...	...	...	5.28(±2.56)e−14	−0.25±0.05
DG Tau	3.89(±3.08)e−14	−3.98±1.56	9.36(±0.90)e−14	−5.23±0.75	...	...	...	...
DL Tau	4.54(±2.60)e−14	−12.04±1.15	6.99(±3.52)e−14	−6.59±3.30	1.35(±1.07)e−14	−1.18±1.00	9.19(±1.86)e−14	−6.81±2.28
HN Tau A	1.61(±0.74)e−14	−4.51±3.50	2.73(±0.89)e−14	−5.35±2.47	...	...	3.70(±1.04)e−14	−5.55±2.26
DO Tau	1.22(±0.43)e−14	−1.27±0.82	2.93(±0.69)e−14	−1.83±0.80	7.47(±5.83)e−15	−0.56±0.50	4.08(±1.23)e−14	−3.00±1.43
RW Aur A	5.41(±1.63)e−13	−2.79±0.99	4.48(±1.99)e−13	−2.18±1.13	1.71(±0.35)e−13	−0.85±0.18	8.33(±1.20)e−13	−3.97±0.81
CQ Tau	...	...	...	...	...	...	...	...

Object	$\log(L_{\mathrm{acc}}/L_{\odot})$ He I λ4026	$\pm\sigma$ (dex)	$\log(L_{\mathrm{acc}}/L_{\odot})$ He I λ4471	$\pm\sigma$ (dex)	$\log(L_{\mathrm{acc}}/L_{\odot})$ He I λ4713	$\pm\sigma$ (dex)	$\log(L_{\mathrm{acc}}/L_{\odot})$ He I λ4922	$\pm\sigma$ (dex)
RY Tau	−0.64	0.30	...	...	...	...	−0.33	0.27
DG Tau	−0.37	0.41	−0.20	0.18	...	...	...	...
DL Tau	−0.25	0.32	−0.27	0.29	−0.73	0.46	−0.32	0.19
HN Tau A	−0.87	0.29	−0.85	0.25	...	...	−0.84	0.22
DO Tau	−0.87	0.26	−0.70	0.22	−0.98	0.46	−0.70	0.22
RW Aur A	+0.61	0.21	+0.34	0.26	+0.04	0.31	+0.42	0.16
CQ Tau	...	...	...	...	...	...	...	...

Table B.4. Measured fluxes and equivalent widths of He I lines and accretion luminosity for the CTTs sample: He I 5016 to He I 10830.

Object	$f_{\text{He I }\lambda5016}$ (erg s^{-1} cm^{-2})	$EW_{\text{He I }\lambda5016}$ (Å)	$f_{\text{He I }\lambda5876}$ (erg s^{-1} cm^{-2})	$EW_{\text{He I }\lambda5876}$ (Å)	$f_{\text{He I }\lambda6678}$ (erg s^{-1} cm^{-2})	$EW_{\text{He I }\lambda6678}$ (Å)	$f_{\text{He I }\lambda10830}$ (erg s^{-1} cm^{-2})	$EW_{\text{He I }\lambda10830}$ (Å)
RY Tau	...	...	1.24(±0.29)e−13	−0.45±0.10	2.09(±0.59)e−14	−0.07±0.05	1.02(±0.10)e−12	−0.25±0.02
DG Tau	...	...	1.27(±0.16)e−13	−3.57±0.61	5.84(±3.57)e−14	−1.17±0.78	1.65(±0.07)e−12	−1.70±0.15
DL Tau	2.55(±0.45)e−14	−1.84±0.56	1.52(±0.18)e−13	−6.55±1.12	5.98(±3.40)e−14	−2.06±1.34	1.21(±0.06)e−12	−2.49±0.22
HN Tau A	1.29(±0.23)e−14	−1.88±0.45	4.23(±0.99)e−14	−4.76±1.44	1.62(±0.94)e−14	−1.53±0.98	3.78(±0.21)e−13	−2.61±0.25
DO Tau	7.44(±1.67)e−15	−0.55±0.18	6.31(±0.72)e−14	−3.02±0.57	2.59(±0.33)e−14	−1.00±0.18	2.04(±0.16)e−13	−0.59±0.08
RW Aur A	7.22(±0.72)e−13	−3.20±0.40	5.00(±0.56)e−13	−2.33±0.31	4.72(±0.83)e−13	−2.21±0.45	3.00(±0.24)e−12	−1.91±0.21
CQ Tau	...	...	5.97(±1.70)e−14	−0.15±0.05	8.63(±4.58)e−15	−0.03±0.02	4.92(±0.67)e−13	−0.22±0.04

Object	$\log(L_{\text{acc}}/L_{\odot})$ He I $\lambda5016$	$\pm\sigma$ (dex)	$\log(L_{\text{acc}}/L_{\odot})$ He I $\lambda5876$	$\pm\sigma$ (dex)	$\log(L_{\text{acc}}/L_{\odot})$ He I $\lambda6678$	$\pm\sigma$ (dex)	$\log(L_{\text{acc}}/L_{\odot})$ He I $\lambda10830$	$\pm\sigma$ (dex)
RY Tau	...	...	−0.14	0.21	−0.57	0.32	−0.63	0.38
DG Tau	...	...	−0.42	0.19	−0.29	0.43	−0.54	0.36
DL Tau	−0.54	0.21	−0.22	0.19	−0.13	0.41	−0.50	0.36
HN Tau A	−0.97	0.22	−1.03	0.23	−1.02	0.44	−1.24	0.43
DO Tau	−1.10	0.23	−0.72	0.20	−0.66	0.30	−1.47	0.46
RW Aur A	+0.71	0.16	+0.19	0.18	+0.83	0.25	−0.02	0.33
CQ Tau	...	...	−1.11	0.25	−1.58	0.43	−1.13	0.42

Table B.5. Measured fluxes and equivalent widths of the Ca I $\lambda3934$ line and accretion luminosity for the CTTs sample.

Object	$f_{\mathrm{Ca\,I}\,\lambda3934}$ (erg s^{-1} cm^{-2})	$EW_{\mathrm{Ca\,I}\,\lambda3934}$ (Å)	$\log(L_{\mathrm{acc}}/L_{\odot})$ Ca I $\lambda3934$	$\pm\sigma$ (dex)
RY Tau	2.57(±0.29)e−13	-6.61±2.97	−0.26	0.16
DG Tau	7.45(±0.72)e−13	-40.05±16.00	−0.12	0.15
DL Tau	2.43(±0.39)e−13	-56.38±15.00	−0.57	0.17
HN Tau A	3.29(±0.49)e−13	-94.81±25.50	−0.58	0.17
DO Tau	2.14(±0.49)e−13	-25.94±10.40	−0.66	0.19
RW Aur A	2.72(±0.33)e−12	-13.27±2.86	+0.24	0.15
CQ Tau	3.30(±0.64)e−13	-2.71±0.70	−0.95	0.19